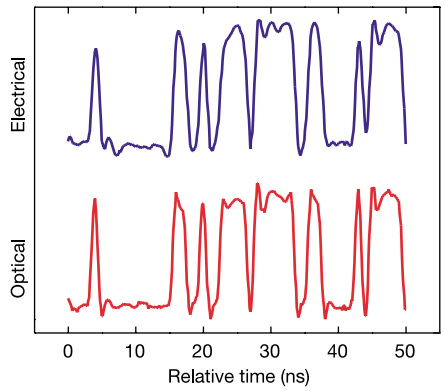

Figure 5 Pseudorandom bit sequence of a silicon Mach–Zehnder interferometer modulator containing a single 2.5-mm-long MOS capacitor phase shifter in one arm at a data bit rate of 1 Gbit s^{-1}.

higher than that of traditional current-injection-based p–i–n diode devices[10,11].

We also investigated the data transmission performance of the MZI modulator with a digital pulse drive voltage. We applied 3.5-V digital pulse pattern with a d.c. bias of 3 V to the phase shifter. With a pseudorandom electrical data input, we detected the corresponding MZI optical output by using a high-frequency photoreceiver. In Fig. 5 we show a 1 Gbit s^{-1} pseudorandom electrical bit sequence input and the corresponding optical output of our modulator. The data show that the optical signal faithfully reproduces the 1 Gbit s^{-1} electrical data stream.

As mentioned above, our current MZI modulator has an on-chip loss of ~ 6.7 dB, which is primarily due to the doped and undoped polysilicon regions in the waveguide. Because the polysilicon has a much larger optical loss than single-crystal silicon[18,19], we could significantly reduce the present modulator loss by replacing the polysilicon region with single-crystal silicon. For the device in Fig. 1, modelling suggests that we could reduce the on-chip loss by ~5 dB by this method. Using the epitaxial lateral overgrowth technique[24], single-crystal silicon can be fabricated over the gate oxide. Investigation of the replacement of polysilicon by single-crystal silicon is under way. Furthermore, because the phase shifter loss depends on the device length, that is, L_π (the active waveguide length required for π phase shift), increasing the phase modulation efficiency (or decreasing the $V_\pi L$ product) by reducing the waveguide dimension and making the gate oxide thinner not only reduces the device size but also the optical loss. Scaling down the waveguide helps the high-frequency operation, as the capacitance is reduced by the device size shrinkage. In addition, reducing the gate oxide thickness and commensurately reducing the drive voltage also reduces the high-frequency power dissipation of the modulator, as with the conventional CMOS circuits[25]. We could also design and fabricate a graded doping profile in the y direction (Fig. 1) in the waveguide phase shifter to further reduce the optical loss, while still maintaining the device speed. For example, we could design a phase shifter with higher doping densities in the areas close to the gate oxide and metal contacts, but with lower doping concentrations in the rest of the waveguide. □

Received 22 September; accepted 18 December 2003; doi:10.1038/nature02310.

1. Soref, R. A. Silicon-based optoelectronics. *Proc. IEEE* **81,** 1687–1706 (1993).
2. Zucker, J. E., Jones, K. L., Miller, B. I. & Koren, U. Miniature Mach-Zehnder InGaAsP quantum well waveguide interferometers for 1.3 μm. *IEEE Photon. Technol. Lett.* **2,** 32–34 (1990).
3. Cites, J. S. & Ashley, P. R. High-performance Mach-Zehnder modulators in multiple quantum well GaAs/AlGaAs. *J. Lightwave Technol.* **12,** 1167–1173 (1992).
4. Fetterman, M., Chao, C.-P. & Forrest, S. R. Fabrication and analysis of high-contrast InGaAsP-InP Mach-Zehnder modulators for use at 1.55-μm wavelength. *IEEE Photon. Technol. Lett.* **8,** 69–71 (1996).
5. Leclerc, O. *et al.* Polarisation-independent InP push-pull Mach-Zehnder modulator for 20 Gbit/s soliton regeneration. *Electron. Lett.* **34,** 1011–1013 (1998).
6. Ido, T. *et al.* Ultra-high-speed multiple-quantum-well electro-absorption optical modulators with integrated waveguides. *J. Lightwave Technol.* **14,** 2026–2034 (1996).
7. Fujiwara, T., Watanabe, A. & Mori, H. Measurement of uniformity of driving voltage in Ti:$LiNbO_3$ waveguides using Mach-Zehnder interferometers. *IEEE Photon. Technol. Lett.* **2,** 260–261 (1990).
8. Wooten, E. L. *et al.* A review of lithium niobate modulators for fiber-optic communications systems. *IEEE J. Select. Topics Quant. Electron.* **6,** 69–82 (2000).
9. Howerton, M. M., Moeller, R. P., Greenblatt, A. S. & Krahenbuhl, R. Fully packaged, broad-band $LiNbO_3$ modulator with low drive voltage. *IEEE Photon. Technol. Lett.* **12,** 792–794 (2000).
10. Tang, C. K. & Reed, G. T. Highly efficient optical phase modulator in SOI waveguides. *Electron. Lett.* **31,** 451–452 (1995).
11. Dainesi, P. *et al.* CMOS compatible fully integrated Mach-Zehnder interferometer in SOI technology. *IEEE Photon. Technol. Lett.* **12,** 660–662 (2000).
12. Png, C. E., Reed, G. T., Atta, R. M. H., Ensell, G. J. & Evans, A. G. R. Development of small silicon modulators in silicon-on-insulator (SOI). *Proc. SPIE* **4997,** 190–197 (2003).
13. Irace, A., Breglio, G. & Cutolo, A. All-silicon optoelectronic modulator with 1 GHz switching capability. *Electron. Lett.* **39,** 232–233 (2003).
14. Soref, R. A. & Lorenzo, P. J. All-silicon active and passive guided-wave components for $\lambda = 1.3$ and 1.6 μm. *IEEE J. Quant. Electron.* **QE-22,** 873–879 (1986).
15. Soref, R. A. & Bennett, B. R. Electrooptical effects in silicon. *IEEE J. Quant. Electron.* **QE-23,** 123–129 (1987).
16. Cutolo, A., Iodice, M., Spirito, P. & Zeni, L. Silicon electro-optic modulation based on a three terminal device integrated in a low-loss single-mode SOI waveguide. *J. Lightwave Technol.* **15,** 505–518 (1997).
17. Sciuto, A., Libertino, S., Alessandria, A., Coffa, S. & Coppola, G. Design, fabrication, and testing of an integrated Si-based light modulator. *J. Lightwave Technol.* **21,** 228–235 (2003).
18. Liao, L. *et al.* Optical transmission losses in polycrystalline silicon strip waveguides: effects of waveguide dimensions, thermal treatment, hydrogen passivation, and wavelength. *J. Electron. Mater.* **29,** 1380–1386 (2000).
19. Liao, L. *Low Loss Polysilicon Waveguides for Silicon Photonics.* Thesis, MIT (1997).
20. Sze, S. M. *Physics of Semiconductor Devices* 2nd edn (Wiley, New York, 1981).
21. Soref, R. A. & Bennett, B. R. Kramers-Kronig analysis of electro-optical switching in silicon. *Proc. SPIE* **704,** 32–37 (1986).
22. Bank, R. E., Rose, D. J. & Fichtner, W. Numerical methods for semiconductor device simulation. *IEEE Trans. Electron. Dev.* **ED-30,** 1031–1041 (1983).
23. Sudbo, A. S. Numerically stable formulation of the transverse resonance method for vector mode-field calculations in dielectric waveguides. *IEEE Photon. Technol. Lett.* **5,** 342–344 (1993).
24. Ahmed, S. S., Denton, J. P. & Neudeck, G. W. Nitrided thermal SiO_2 for use as top and bottom gate insulators in self-aligned double gate silicon-on-insulator metal-oxide-semiconductor field effect transistor. *J. Vac. Sci. Technol. B* **19,** 800–806 (2001).
25. Davari, B., Dennard, R. H. & Shahidi, G. G. CMOS scaling for high performance and low power—The next ten years. *Proc. IEEE* **83,** 595–606 (1995).

Acknowledgements We thank M. Salib for help in process design and optical loss testing; M. Morse, A. Barkai, S. Tubul and D. Tran for technical assistance in device fabrication; A. Alduino for backend processing; and S. Koehl for data collection software. Special thanks go to D. Elqaq, M. Gill, S. Pang and B. Venkateshwaran for contributions during the early stages of this research. Finally, we thank G. Reed for discussions.

Competing interests statement The authors declare that they have no competing financial interests.

Correspondence and requests for materials should be addressed to A.L. (ansheng.liu@intel.com).

A 1.7-kilobase single-stranded DNA that folds into a nanoscale octahedron

William M. Shih[1], Joel D. Quispe[2] & Gerald F. Joyce[1]

[1]*Departments of Chemistry and Molecular Biology and The Skaggs Institute for Chemical Biology, The Scripps Research Institute, 10550 North Torrey Pines Road, La Jolla, California 92037, USA*
[2]*Department of Cell Biology, The Scripps Research Institute, 10550 North Torrey Pines Road, La Jolla, California 92037, USA*

Molecular self-assembly offers a means of spontaneously forming complex and well-defined structures from simple components. The specific bonding between DNA base pairs has been used in this way to create DNA-based nanostructures and to direct the assembly of material on the subnanometre to micrometre scale[1,2]. In principle, large-scale clonal production of suitable DNA sequences and the directed evolution of sequence lineages

©2004 Nature Publishing Group

towards optimized behaviour[3] can be realized through exponential DNA amplification by polymerases. But known examples of three-dimensional geometric DNA objects[4–6] are not amenable to cloning because they contain topologies that prevent copying by polymerases[1,2,7]. Here we report the design and synthesis of a 1,669-nucleotide, single-stranded DNA molecule that is readily amplified by polymerases and that, in the presence of five 40-mer synthetic oligodeoxynucleotides, folds into an octahedron structure by a simple denaturation–renaturation procedure. We use cryo-electron microscopy to show that the DNA strands fold successfully, with 12 struts or edges joined at six four-way junctions to form hollow octahedra approximately 22 nanometres in diameter. Because the base-pair sequence of individual struts is not repeated in a given octahedron[8,9], each strut is uniquely addressable by the appropriate sequence-specific DNA binder.

Rigid DNA structures can be constructed from double-helical struts that are linked at flexible joints (for example, branched junctions) by arrangement of the struts in a continuously triangulated frame[2]. DNA tetrahedra[6] have an architecture that resists deformation, whereas non-triangulated objects, such as DNA cubes[4] and truncated octahedra[5], do not. A DNA regular octahedron, also continuously triangulated, has been proposed previously[10]. Some viruses fold parts of their single-stranded RNA genomes into triangulated (for example, icosahedral[11]) or untriangulated (for example, dodecahedral[12]) geometric shapes, with encapsulating protein shells enforcing these RNA structures.

The DNA octahedron reported here consists of five double-crossover[10] (DX) struts and seven paranemic-crossover[13] (PX) struts, joined at six four-way junctions (Fig. 1a). DX and PX motifs have both been modelled as pairs of double helices that are arranged in a side-by-side manner. Each of the twelve struts of the octahedron contributes one double helix to a 'core' layer and the other to a concentric 'peripheral' layer. The four-way junctions connect only the core-layer double helices. Each four-way junction displays on its concave face the minor grooves of its four proximally surrounding base pairs. All four strands at all six junctions contain two unpaired thymidine residues at the crossover point to allow some flexibility for assembly.

The core-layer double helix of each of the twelve struts contains 40 base pairs, corresponding to roughly four turns of DNA and a length of ~14 nm. For eleven of the struts, the peripheral-layer double helix contains 30 or 32 base pairs and is capped at both helical ends by a hairpin loop of four thymidine residues. The twelfth strut is slightly longer, containing 35 base pairs, and is capped at only one end. DX motifs have been shown to be about twice as stiff as standard duplex DNA[14]. Assuming that PX motifs have similar rigidity, each of the struts would be expected to have a stiffness corresponding to a rod that is roughly one-eighth of a persistence length. Thus the folded octahedron, in which all twelve struts come together, is expected to be a highly rigid object.

Each DX motif contains 20 base pairs between the two crossover junctions, where the strands exchange between the two component double helices. The crossover junctions are flanked on the core-layer helix by eight base pairs on one side and twelve base pairs on the other side, and are flanked on the peripheral-layer helix by either five or six base pairs on each side. Each PX motif contains six crossover junctions separated by three major-groove spacings of six base pairs alternating with two minor-groove spacings of four base pairs. The outermost crossover junctions are flanked on the core-layer helix by seven base pairs on either side, and are flanked on the peripheral-layer helix by three base pairs on either side.

The DNA octahedron was folded from a mixture of a 1,669-nucleotide 'heavy chain' and five 40-nucleotide 'light chains' by heat denaturation followed by successive cooling steps. Folding was designed to occur in two stages. First, the heavy chain and the five light chains associate stoichiometrically and collapse into a branched-tree structure (Fig. 1b). Binding of the heavy and light chains forms double crossovers that provide five of the twelve struts of the target structure. This intermediate state has fourteen terminal branches, each corresponding to a half-strut. The terminal branches are unique 76-nucleotide loops, each with sequence complementarity (in the PX sense) to one and only one other loop sequence (Fig. 1c). In the second stage of folding, conjugate terminal branches associate to form the remaining seven struts. The order of formation of the struts should not make a difference in achieving the final structure.

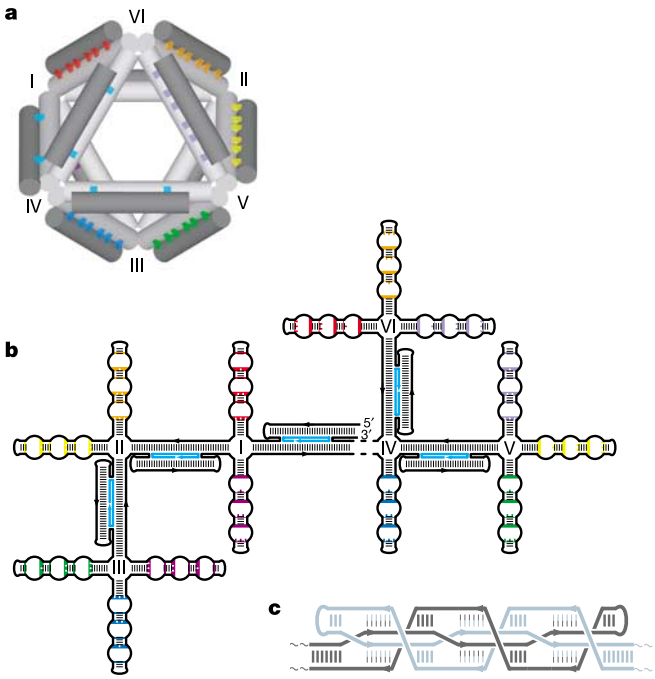

Figure 1 Design of the DNA octahedron. **a**, Three-dimensional structure involving twelve struts (octahedron edges) connected by six flexible joints (octahedron vertices). Five of the struts are DX motifs (cyan) and seven are PX motifs (rainbow colours). The joints are four-way junctions that connect the core-layer double helices of each strut. **b**, Secondary structure of the branched-tree folding intermediate. The structure consists of a single heavy chain (black) and five unique light chains (cyan). Like colours indicate half-PX loops whose sequence-specific cross-association generates a strut that serves as an edge of the DNA octahedron. Coloured stripes coincide with strand crossover positions. Folding to the structure in the upper left is complete when all seven PX struts have formed. **c**, Schematic of a PX strut.

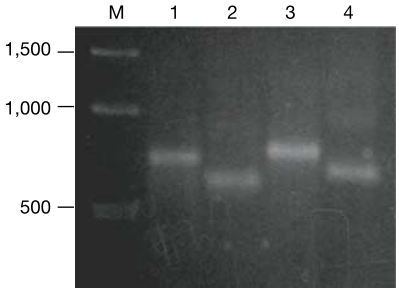

Figure 2 Gel-shift analysis of folding of the DNA octahedron. Lane M, marker lane with DNA size standards (number of base pairs indicated at the left). Lane 1, heavy chain folded in the absence of Mg^{2+}. Lane 2, heavy chain folded in the presence of Mg^{2+}. Lane 3, heavy and light chains folded in the absence of Mg^{2+}. Lane 4, heavy and light chains folded in the presence of Mg^{2+}. Samples were electrophoresed at 100 V at 4 °C in a 2% agarose gel containing 2 mM $MgCl_2$, 0.5 $\mu g\ ml^{-1}$ ethidium bromide, 45 mM Tris base, and 45 mM boric acid (pH 8.0).

©2004 Nature Publishing Group

The DNA octahedron reported here contains no catenations or knots. Therefore no covalent bonds need to be formed or broken to attain the final structure. It was suggested previously that catenated DNA objects might be formed from a single DNA strand by topoisomerization to establish the required knots followed by restriction digestion and ligation to achieve conversion to a catenane[7], although this has not been demonstrated experimentally. An uncatenated structure, as exemplified by the present study, may be less robust because no covalent bonds need to be broken to sever the edges. Yet this structure was preferred because it can be formed by a simple folding protocol.

An initial test for proper folding was provided by a gel mobility-shift assay (Fig. 2). During folding in the absence of Mg^{2+}, the half-PX terminal branches should be unable to associate, leaving the DNA object with the extended branched-tree structure. During folding in the presence of Mg^{2+}, the terminal branches should associate to form PX struts, resulting in a more compact structure. Consistent with these expectations, the DNA exhibited an increased gel mobility when folded in the presence of Mg^{2+}compared to its absence. If any of the fourteen half-PX loops had not been satisfied by an intramolecular partner, then they would have been available for pairing with a separate molecule. About half of the material was observed to be monomeric after folding in the presence of Mg^{2+} (Fig. 2, lane 4), suggesting that most of the half-PX loops were satisfied intramolecularly or were otherwise unavailable for intermolecular pairing.

The overall structure of the DNA octahedron was revealed using cryo-electron microscopy and single-particle reconstruction techniques[15–17]. Figure 3a shows a representative cryo-electron micrograph, demonstrating numerous octahedral-shaped objects of the expected size. Some particles in the micrographs do not appear to be properly folded, although the low signal-to-noise ratio of the images makes it difficult to determine what fraction of the particles have adopted the target structure. Distorted particles in the image field could be the result either of misfolding or of rearrangement during preparation for cryo-freezing, perhaps induced by adhesion to the supporting carbon substrate. The best estimate for the fraction of properly folded particles comes from the gel mobility-shift data (Fig. 2), which suggests that about half of the material is properly folded.

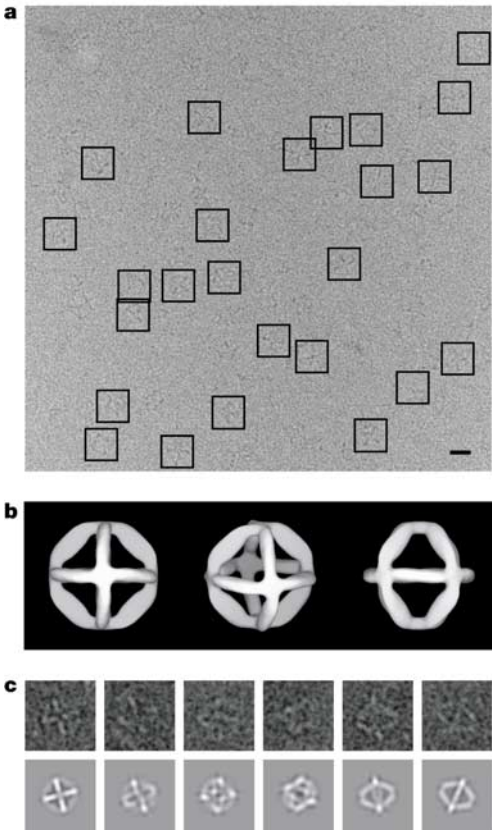

Figure 3 Visualization of the DNA octahedron structure by cryo-electron microscopy. **a**, Representative cryo-electron micrograph, with 25 individual DNA particles boxed. Scale bar, 20 nm. **b**, Three views of the three-dimensional map generated from single-particle reconstruction of the DNA octahedron. **c**, Raw images of individual particles and corresponding projections of the three-dimensional map.

Figure 3b shows a three-dimensional map of the structure of the DNA octahedron, reconstructed from 961 particles. The signal-to-noise ratio was too low to allow meaningful reconstruction without imposing some form of symmetry. Initially, four-fold rotational symmetry was imposed, which produced a map with an octahedral shape. Then a second reconstruction was performed imposing octahedral symmetry, resulting in a better-defined structure. Decoy reconstructions were performed imposing other symmetries (for example, D3, C5, D5, C6), but all of these produced a map whose projections match poorly with the corresponding class averages, whereas there is a close match for the octahedral map (see Supplementary Information). The folded object has the overall shape of an octahedron, but at a fine level it is not perfectly regular because each strut has a different DNA sequence.

Figure 3c shows raw images of representative particles, each accompanied by a corresponding projection of the computed map. The density along the struts in this map demonstrates a paddle shape that is consistent in dimensions with two adjacent double helices having an overall cross-section of about 2 nm × 4 nm. The struts appear to be pinned at four-way joints connected on the inside corners of each strut, consistent with the designed structure of four-way junctions that join core-layer double helices and peripheral-layer double helices that lie outside the framework defined by the core layer. The cavity enclosed by the struts is large enough to accommodate a sphere having a diameter up to 14 nm, while the triangular opening on each face is large enough to allow passage of a sphere having a diameter of up to 8 nm.

Formation of an octahedron structure from the branched-tree intermediate could in principle follow an erroneous course, in which the four-way junctions fold with the major instead of minor grooves of the surrounding base pairs on the concave face of each junction. In this misfolded isomer, the double helices that are not connected by four-way junctions (corresponding to the peripheral-layer helices of the correct isomer) would lie on the inside of the octahedron. Severe steric clashes seem to prevent this alternative isomer from forming.

The assembly strategy presented here could be modified to produce catenated structures, such as the DNA cube[4] reported previously, by substituting hairpin loops that encode restriction sites for the half-PX loops. Cleavage of the restriction sites would produce sticky ends that could be ligated to their appropriate partners. The requirement for light chains could be eliminated by replacing DX struts with simple duplex struts. DX struts were preferred here to produce an octahedron with greater rigidity and pseudosymmetry.

This study has demonstrated that a long single-stranded DNA, accompanied by five synthetic 40-mer oligodeoxynucleotides, can fold without knotting into a DNA cage having the form of an octahedron. The heavy-chain DNA can be amplified in the context of a bacterial plasmid and later excised, allowing its clonal production. The DNA octahedron can be modified in a modular fashion by extending the ends of any of the peripheral double helices or by making insertions into the struts. Sequence variants, perhaps displaying variable loops at multiple locations on the DNA scaffold, could be used to initiate directed evolution studies.

Manipulation of the basic octahedron structure could produce a family of scaffold variants whose function is to position other

©2004 Nature Publishing Group

material at uniquely defined locations. Just as messenger RNAs encode the one-dimensional positioning of transfer-RNA adaptors along their lengths, rigid DNA nanostructures could encode the positioning of sequence-specific DNA binders along their three-dimensional frameworks. DNA nanostructures, therefore, can be regarded as devices that use molecular recognition to translate sequence information into three-dimensional positions. The demonstration of a clonable DNA octahedron is a step towards making the translation of DNA sequence information into position more practical and more versatile. □

Methods

Design of sequences

PX sequences were chosen as will be described elsewhere (W.M.S. & G.F.J., manuscript in preparation). DX sequences were chosen arbitrarily, using the model junction J1[18] for the crossover junctions. The DX sequences were examined to eliminate any seven-nucleotide repeats. Folding of the assembled heavy chain was analysed using MFOLD[19]. Iterative changes were made to the sequence until the target branched-tree structure was achieved as the lowest-energy output.

Folding conditions

Folding was achieved by incubation at 90 °C for 5 min, 65 °C for 20 min, 55 °C for 20 min, 45 °C for 20 min, and 37 °C for 30 min. The folding mixture contained 100 nM heavy chain, 400 nM each of the five light chains, 10 mM $MgCl_2$, 50 mM NaCl, and 40 mM EPPS (pH 7.5).

Synthesis, cloning, and purification of single-stranded DNA

The 1,669-nucleotide heavy chain was constructed by polymerase chain reaction (PCR)-based assembly[20], using synthetic oligodeoxynucleotides prepared by standard phosphoramidite chemistry on a PerSeptive Biosystems Expedite 8900 automated DNA synthesizer. The PCR products were gel purified and ligated into pBS II KS^+ plasmids, which were transformed into *Escherichia coli* (see Supplementary Information for additional details). Multiple clones were selected and sequenced to identify error-free clones. An *Eco*R V site was placed upstream and an N.*Bbv*C IA (nicking endonuclease) site was placed downstream of the heavy-chain sequence using the Stratagene Quikchange cloning kit. The plasmid was amplified in *E. coli* and purified using the QIAGEN QiaQuick ion-exchange chromatography system. The desired single strand was obtained by excision with *Eco*R V and *N.Bbv*C IA, then purified by electrophoresis in a 1.5% alkaline agarose gel, and further purified by electrophoresis in a 1.5% native agarose gel. The light chains were prepared by chemical synthesis. The sequences of all oligodeoxynucleotides used in this study are provided in the Supplementary Information.

Electron microscopy

Cryo-electron microscopy was performed as described[15]. A 4-μl drop of folded DNA, concentrated to 500 nM by microdialysis, was placed on a 300-mesh copper grid covered with a continuous carbon substrate and glow-discharged in amyl amine. The grid was blotted for ~2 s with Whatman filter paper no. 1 and plunge-frozen into liquid ethane. The specimen was observed at −176 °C using a Gatan 626 cryo-stage on a Philips Tecnai F20 FEG operating at 120 kV. Paired images at approximately 0.6 and 2.0 μm defocus were recorded on a Tietz 2k × 2k charge-coupled device (CCD) camera under low-dose conditions using the Leginon[21] automated data collection software system. The magnification was ×62,000, resulting in a pixel size of 2.24 Å. The best 961 images of boxed particles at 2.0-μm defocus were used for three-dimensional reconstruction using the program EMAN[22]. For verification, a second set of paired images was collected and used to carry out an independent reconstruction (see Supplementary Information).

An initial model was generated using 120 particles and the EMAN program 'startoct'. This model was used to produce a set of projections with an angular interval of 3°. The images were aligned with these reference projections to determine the origins and orientations, and a three-dimensional reconstruction was calculated. Cycles of angular refinement were performed with an angular interval of 3° until convergence, with a total of 665 particles contributing to the final average map. Full octahedral symmetry was imposed during the reconstruction. To evaluate the quality of the reconstruction, the data were divided into two groups, and two independent reconstructions were calculated. The resolution of the final reconstruction was estimated as 32 Å, where the Fourier shell correlation between the two independent reconstructions started to fall below 0.5. Maps were rendered using the UCSF Chimera package[23].

Received 8 October; accepted 18 December 2003; doi:10.1038/nature02307.

1. Seeman, N. C. DNA in a material world. *Nature* **421,** 427–431 (2003).
2. Seeman, N. C. DNA nanotechnology: novel DNA constructions. *Annu. Rev. Biophys. Biomol. Struct.* **27,** 225–248 (1998).
3. Wilson, D. S. & Szostak, J. W. *In vitro* selection of functional nucleic acids. *Annu. Rev. Biochem.* **68,** 611–647 (1999).
4. Chen, J. H. & Seeman, N. C. Synthesis from DNA of a molecule with the connectivity of a cube. *Nature* **350,** 631–633 (1991).
5. Zhang, Y. & Seeman, N. C. The construction of a DNA truncated octahedron. *J. Am. Chem. Soc.* **116,** 1661–1669 (1994).
6. Dorenbeck, A.. *DNA Nanostructures by Self-Assembly of Trisoligonucleotidyls*. Thesis, Univ. Bochum (2000).
7. Seeman, N. C. Construction of three-dimensional stick figures from branched DNA. *DNA Cell Biol.* **10,** 475–486 (1991).
8. Seeman, N. C. Nucleic-acid junctions and lattices. *J. Theor. Biol.* **99,** 237–247 (1982).
9. Seeman, N. C. *De novo* design of sequences for nucleic acid structural engineering. *J. Biomol. Struct. Dyn.* **8,** 573–581 (1990).
10. Li, X. J., Yang, X. P., Qi, J. & Seeman, N. C. Antiparallel DNA double crossover molecules as components for nanoconstruction. *J. Am. Chem. Soc.* **118,** 6131–6140 (1996).
11. Larson, S. B. *et al.* Double-helical RNA in satellite tobacco mosaic virus. *Nature* **361,** 179–182 (1993).
12. Tang, L. *et al.* The structure of Pariocoto virus reveals a dodecahedral cage of duplex DNA. *Nature Struct. Biol.* **8,** 77–83 (2001).
13. Zhang, X., Yan, H., Shen, Z. & Seeman, N. C. Paranemic cohesion of topologically-closed DNA molecules. *J. Am. Chem. Soc.* **124,** 12940–12941 (2002).
14. Sa-Ardyen, P., Vologodskii, A. V. & Seeman, N. C. The flexibility of DNA double crossover molecules. *Biophys. J.* **84,** 3829–3837 (2003).
15. Dubochet, J. *et al.* Cryo-electron microscopy of vitrified specimens. *Q. Rev. Biophys.* **21,** 129–228 (1988).
16. Frank, J. Averaging of low exposure electron micrographs of non-periodic objects. *Ultramicroscopy* **1,** 159–162 (1975).
17. Frank, J. Classification of macromolecular assemblies studied as 'single particles'. *Q. Rev. Biophys.* **23,** 281–329 (1990).
18. Seeman, N. C. & Kallenbach, N. R. Design of immobile nucleic acid junctions. *Biophys. J.* **44,** 201–209 (1983).
19. Zuker, M. Mfold web server for nucleic acid folding and hybridization prediction. *Nucleic Acids Res.* **31,** 1–10 (2003).
20. Stemmer, W. P., Crameri, A., Ha, K. D., Brennan, T. M. & Heyneker, H. L. Single-step assembly of a gene and entire plasmid from large numbers of oligodeoxyribonucleotides. *Gene* **64,** 49–53 (1995).
21. Carragher, B. *et al.* Leginon: an automated system for acquisition of images from vitreous ice specimens. *J. Struct. Biol.* **132,** 33–45 (2000).
22. Ludtke, S. J., Baldwin, P. R. & Chiu, W. EMAN: semiautomated software for high-resolution single-particle reconstructions. *J. Struct. Biol.* **128,** 82–97 (1999).
23. Huang, C. C., Couch, G. S., Pettersen, E. F. & Ferrin, T. E. Chimera: An extensible molecular modeling application constructed using standard components. *Pacif. Symp. Biocomput.* **1,** 724 (1996).

Supplementary Information accompanies the paper on **www.nature.com/nature**.

Acknowledgements We thank F. Guerra for help with EMAN reconstructions and B. Carragher, R. Milligan and C. Potter for advice on reconstructions. This work was supported by the National Aeronautics and Space Administration and The Skaggs Institute for Chemical Biology at The Scripps Research Institute. Some of the work presented here was conducted at the National Resource for Automated Molecular Microscopy, which is supported by the National Institutes of Health through the National Center for Research Resources. W.M.S. is a Fellow supported by the Damon Runyon Cancer Research Foundation. Molecular graphics images were produced using the UCSF Chimera package.

Competing interests statement The authors declare that they have no competing financial interests.

Correspondence and requests for materials should be addressed to W.M.S. (wmshih@scripps.edu).

Earthquake nucleation by transient deformations caused by the *M* = 7.9 Denali, Alaska, earthquake

J. Gomberg[1], P. Bodin[2], K. Larson[3] & H. Dragert[4]

[1]*US Geological Survey, Center for Earthquake Research and Information, 3876 Central Ave. Suite 2, and* [2]*Center for Earthquake Research and Information, The University of Memphis, 3876 Central Ave. Suite 1, Memphis, Tennessee 38152-3050, USA*
[3]*Department of Aerospace Engineering Sciences, University of Colorado at Boulder, Boulder, Colorado 80309-0429, USA*
[4]*Geological Survey of Canada, Pacific Geoscience Centre, 9860 West Saanich Road, Sidney, British Columbia, V8L 4B2, Canada*

The permanent and dynamic (transient) stress changes inferred to trigger earthquakes are usually orders of magnitude smaller than the stresses relaxed by the earthquakes themselves, implying that triggering occurs on critically stressed faults[1–4]. Triggered seismicity rate increases may therefore be most likely to occur in areas where loading rates are highest and elevated pore pressures,

©2004 Nature Publishing Group